6 The influence of erosion on bivergent wedge evolution

The following chapter intends to elucidate the influence of the location of erosion with respect to the convergence geometry and the mode of erosion, i. e., distributed or focused on the kinematic evolution of bivergent sand-wedges. Thereby, special emphasis is devoted to finite strain accumulation, the topographic evolution and to the geometry of particle paths. A summary of experiment 9.05, which is used as reference, is provided first, followed by a description of four experiments which differ only with respect to the mode and location of erosion (Fig. 6.1).

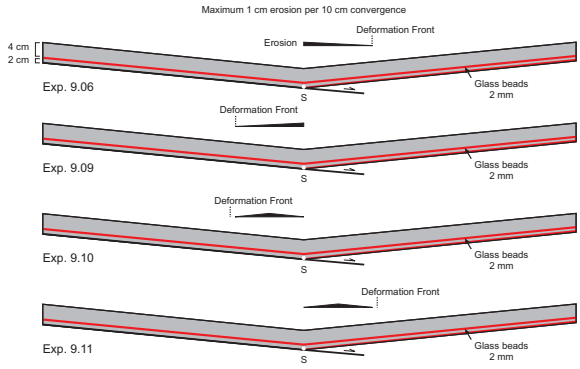

Figure 6.1: Kinematic boundary conditions and erosion modes of 2^{nd} experimental series. Distributed erosion of: (a) Retro-wedge, (b) Pro-wedge; Focused erosion of: (c) Pro-wedge, (d) Retro-wedge.

6.1 Reference experiment without erosion

The following section summarises the results obtained from experiment 9.05 and the reader is referred to section (5.2), where a detailed account on this experiment is provided.

Visual inspection of experiment 9.05 reveals, as previously noted, a four staged evolution. During stage I initial layer parallel shortening leads to the formation of two conjugate shear zones, which nucleated at the singularity. They define a symmetric pop-up (Fig. 6.2a). Further convergence leads to a rapid uplift associated with progressive back tilting of the pop-up towards the upper plate. In stage II, three narrowly spaced thrust faults are formed within the pro-layer (Fig. 6.2b, c) and result in an increasing asymmetry of wedge topography and kinematics. At this stage rates of thrusting along the retro shear-zone and uplift rates of the axial-zone and the retro-wedge are high but start to decrease (Fig. 6.3a). Stage III commences after $40\,cm$ of convergence (Fig. 6.2d, e). The initial pro-wedge provides now sufficient load to activate the internal glass bead-layer, which facilitates the coeval formation of thrust imbricates above and duplexes below it. Lateral growth of the pro-wedge is now attained by cyclic formation of flat-topped box anticlines at its toe. Coeval to frontal accretion, the sand layer beneath the glass bead-layer is detached from the one above and is as well transferred towards the axial-zone. Beneath the base of the pro-wedge, duplexes are formed, stacked, and finally uplifted in the hangingwall of the retro shear-zone. Thus, compared to the pro-wedge, which grows by discrete steps, the axial-zone and the retro-wedge are continuously fed with pro-wedge derived material. Thereby, the axial-zone and the retro-wedge grow in width and height. These two modes of addition of new material to the respective sub-wedges further amplify the existing topographic and kinematic asymmetry of the bivergent sand-wedge.

While the rates of the lateral growth of the pro-wedge increase during stage III, a further decrease of the rates of thrusting along the retro shear-zone and the uplift rates of both the axial-zone and the retro-wedge is observed (Fig. 6.3a). After $\sim 90\,cm$ of convergence, frontal accretion within the retro-wedge emerges and marks thus the onset

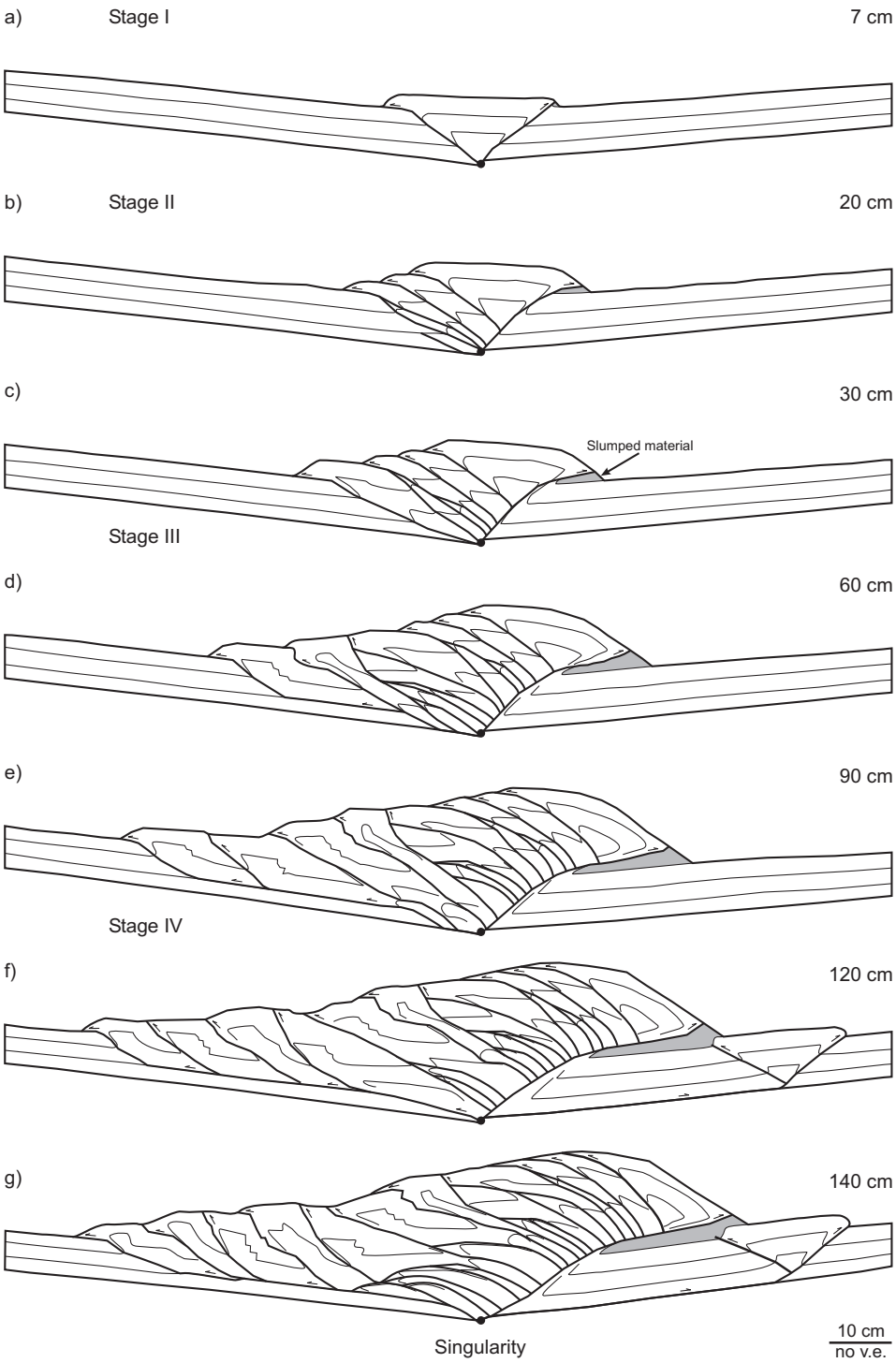

Figure 6.2: Line drawings of sequential stages of experiment (9.05), used as reference for the experiments involving erosion. Numbers on the right are *cm* of convergence. A footwall shortcut can be observed in (c) before deformation propagates far into the undeformed pro-layer and stage (III) begins, i. e., after $40\,cm$ of convergence. Frontal accretion within the upper plate emerges after $\sim 90\,cm$ of convergence, i. e., stage IV commences.

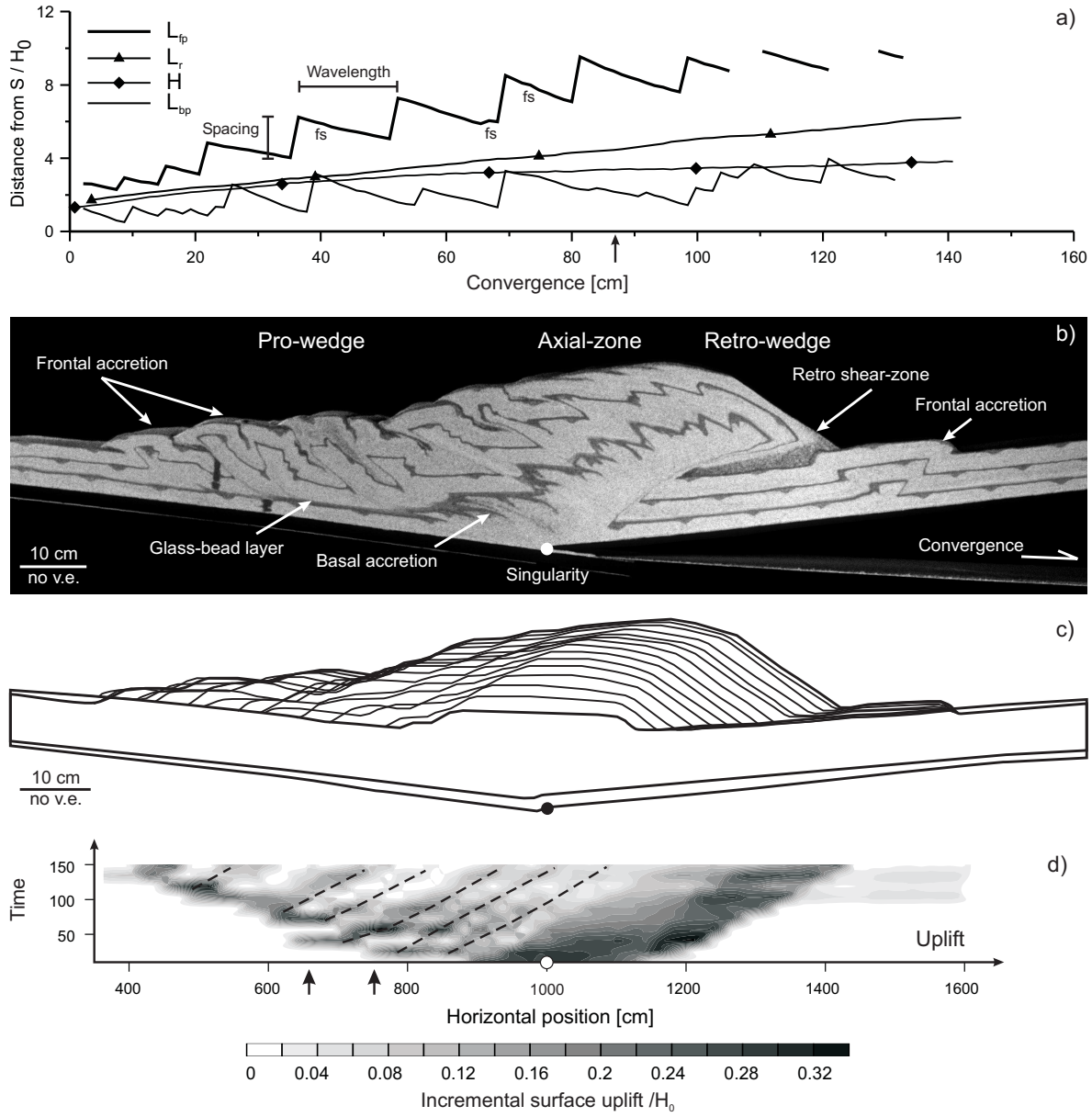

Figure 6.3: Synopsis of reference experiment. (a) Evolution of geometric parameters as defined in figure (4.11), taken from the digital images at every 1.5 *cm* of convergence. Arrow indicates onset of upper plate accretion. fs shows footwall shortcuts. (b) Photograph after 140 *cm* of convergence. (c) Topographic evolution. Outlines were taken at every 10 *cm*. of convergence. The first, i. e., after 10 *cm* and the last, i. e., after 150 *cm* of convergence outline are given in complete form, to indicate the magnitude of flexure. Two growth modes can be distinguished: cyclic accretion within the pro-wedge results in distinct steps in topography, whereas continuous addition of pro-wedge derived material to the axial-zone and the retro-wedge leads to near concentric growth pattern. (d) ISU with high spatial and temporal variability. Arrows indicate positions, where ISU changes by 10 during the evolution of the bivergent sand-wedge. Dashed lines trace activity of ramp segments. (e) From PIV extracted particle paths after 140 *cm* of convergence.

of stage IV. Continued convergence and resulting deformation is now taken up by two frontal and one basal accretion system (Fig. 6.2f, g, Fig. 6.3b). This results in a slowdown of the rate with which the pro-wedge grows laterally (Fig. 6.3a). Key characteristics of the topography and its evolution include: (i) the existence of two uplift domains (Fig. 6.3c); (ii) the uplift trace of the different phases of thrust activity, i. e. the life-cycle of a thrust; (iii) the correlation between maximum ISU within the pro-wedge and significantly lowered ISU within the axial-zone and the retro-wedge for a given time-slice and (iv) the surface uplift waves associated with the accretion cycles (Fig. 6.3d). Also, the onset of frontal accretion within the retro-wedge results in a significant reduction of ISU within the pro-wedge.

6.2 Experiments with erosion

A summary of the similarities between the reference experiment and the experiments involving erosion is provided first, followed by an analysis of the differences between these experiments.

One of the key observations which emerged from the analysis of the PIV images is that despite the differences in the location and the mode of erosion, all sand-wedges evolved into a bivergent state with a pro-wedge, an axial-zone and a retro-wedge (Fig. 6.4). All four bivergent sand-wedges subjected to erosion showed at least the first three phases out of the four stage evolutionary model proposed in section (5.1). Finally, all experiments showed a simultaneous occurrence of frontal and basal accretion and no activation of the internal upper plate glass-bead layer.

Particle paths. For each experiment two triangular markers were traced, which started at approximately the same position. One marker was located above and one below the internal glass-bead layer, as a representation for frontal and basal accretion, respectively. The spatial distribution of both markers after 140 *cm* of convergence indicates:

i. Different magnitudes of displacement between both accretion modes must have occurred, since the distance between both markers varies between experiments (Fig. 6.4a, e). They are closest in the distributed pro-wedge erosion and farthest in the reference experiment (Fig. 6.4a, c).

ii. The markers for frontal accretion reached a similar position in the reference as well as in the retro-wedge erosion experiments (Fig. 6.4a, b, e). However, the markers for basal accretion show a larger displacement, but are located in the same region as the respective marker in the reference experiment (Fig. 6.4a, b, e).

iii. During pro-wedge erosion the markers being representative for frontal accretion indicate a higher displacement and a change in the direction of the particle flow. The markers for basal accretion attained a similar position as observed in the reference experiment (Fig. 6.4a, c, d).

Additionally, up to 120 particles were traced for each experiment (Fig. 6.5). The respective particle path geometries show a flat-ramp-flat geometry and no distinction can be made between frontally and basally accreted particles. Only those particles, derived from the upper or the lower plate can be distinguished. In pro-wedge erosion experiments, particle paths within the axial-zone are slightly steeper than in the retro-wedge erosion or within the reference experiment (Fig. 6.5). This agrees with the previous observation, that pro-wedge erosion redirects particle-flow.

Visual inspection of the photographs (Fig. 6.4) indicates that the internal glass-bead layer was exposed at the surface of the pro-wedge during focused pro-wedge erosion, which did not occur in

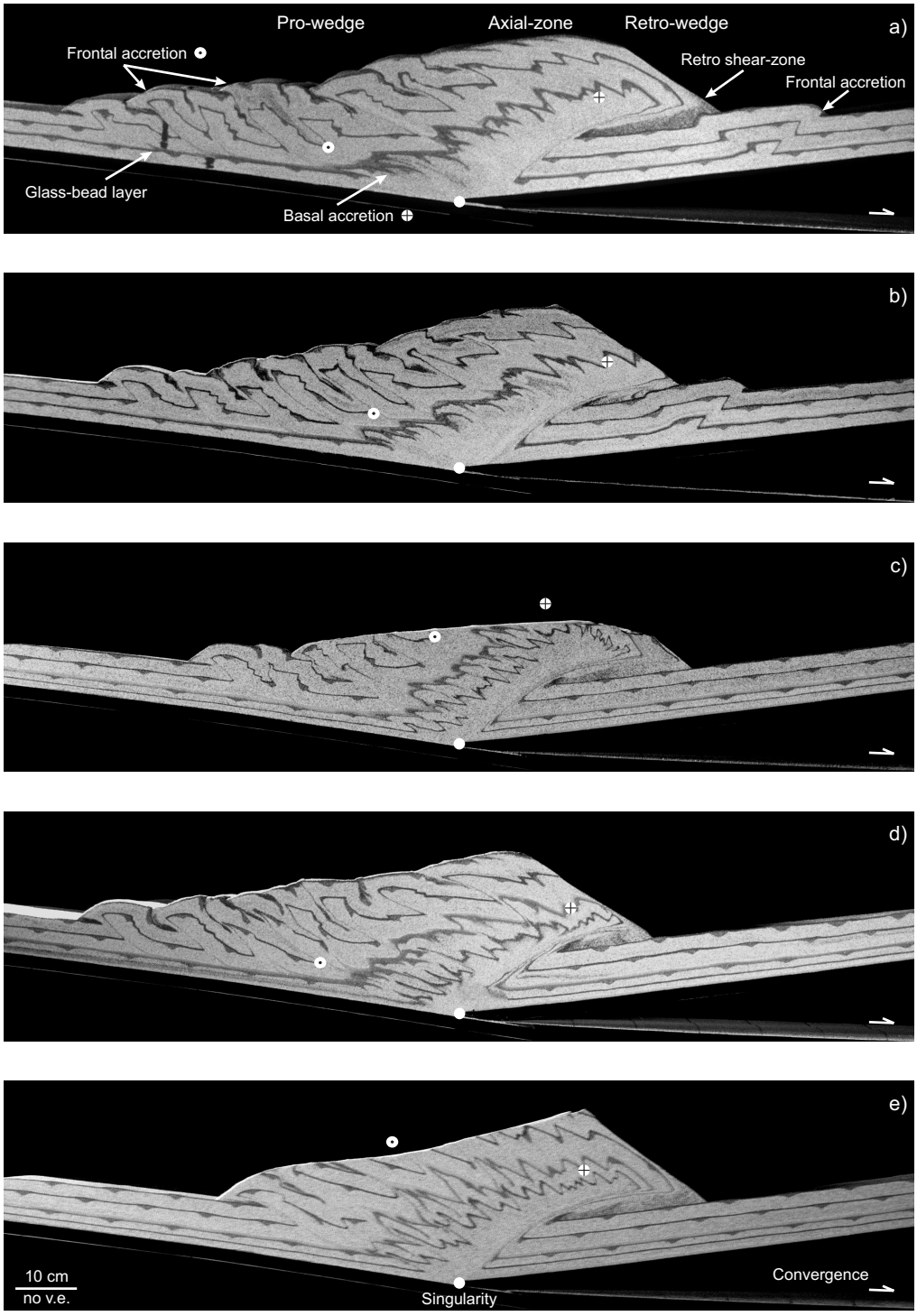

Figure 6.4: Photographic images of each experiment after 140 *cm* of convergence. (a) Reference experiment; Distributed erosion of: (b) Retro-wedge, (c) Pro-wedge; Focused erosion of: (d) Retro-wedge, (e) Pro-wedge. The main structural elements are highlighted. Two markers, one being indicative for the frontal accretion (black dot), the other being indicative for the basal accretion (black cross) are given to show different amount of exhumation.

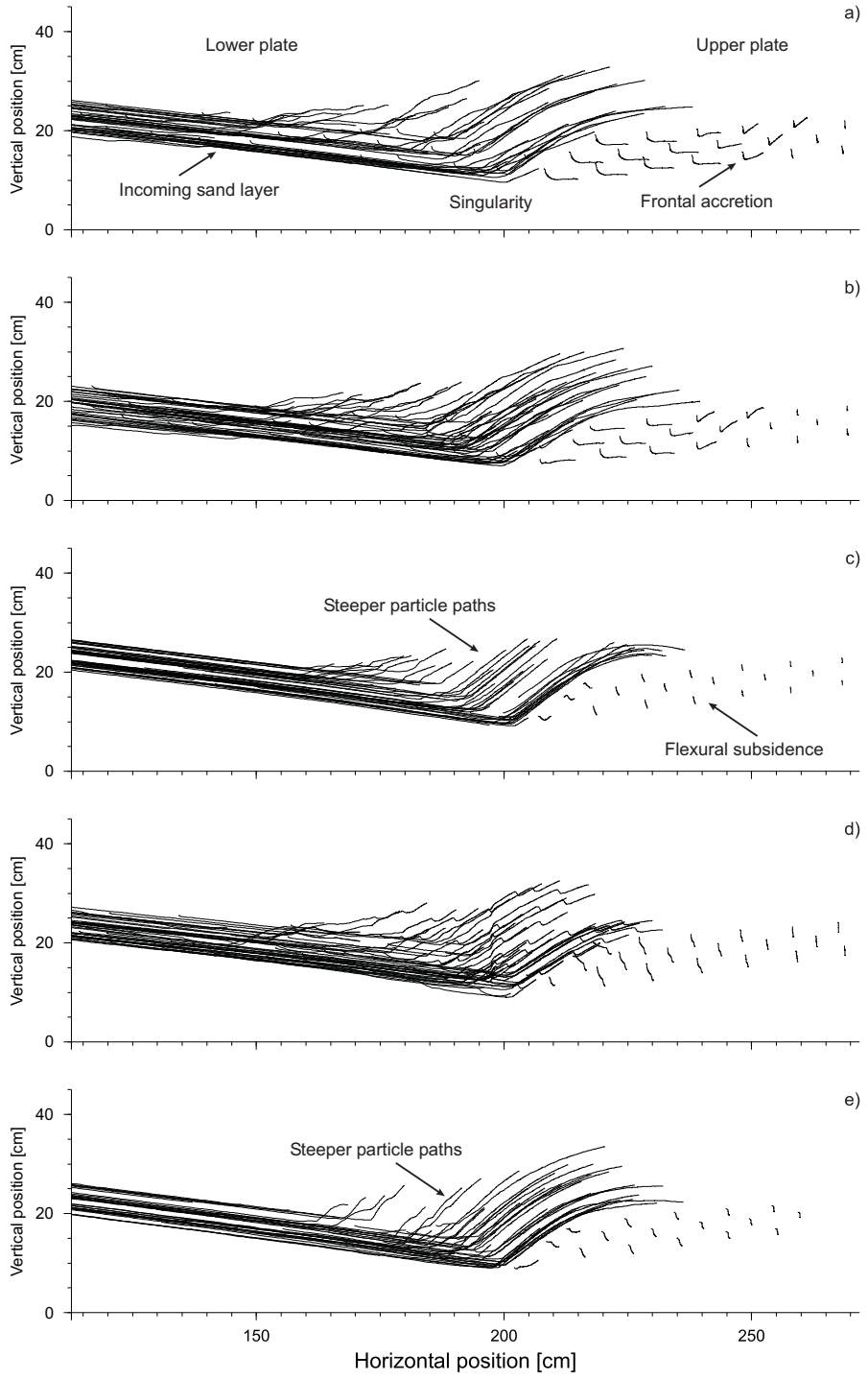

Figure 6.5: Particle paths calculated for ~ 120 particles for each experiment. (a) Reference experiment; Distributed erosion of: (b) Retro-wedge, (c) Pro-wedge; Focused erosion of: (d) Retro-wedge, (e) Pro-wedge. All particle paths show a flat-ramp-flat geometry. There is no difference in particle path geometry between frontally and basally accreted particles. Particle paths within the axial-zone are slightly steeper in pro-wedge erosion experiments (c, e), which indicates that pro-wedge erosion tends to redirect the tectonic mass flux.

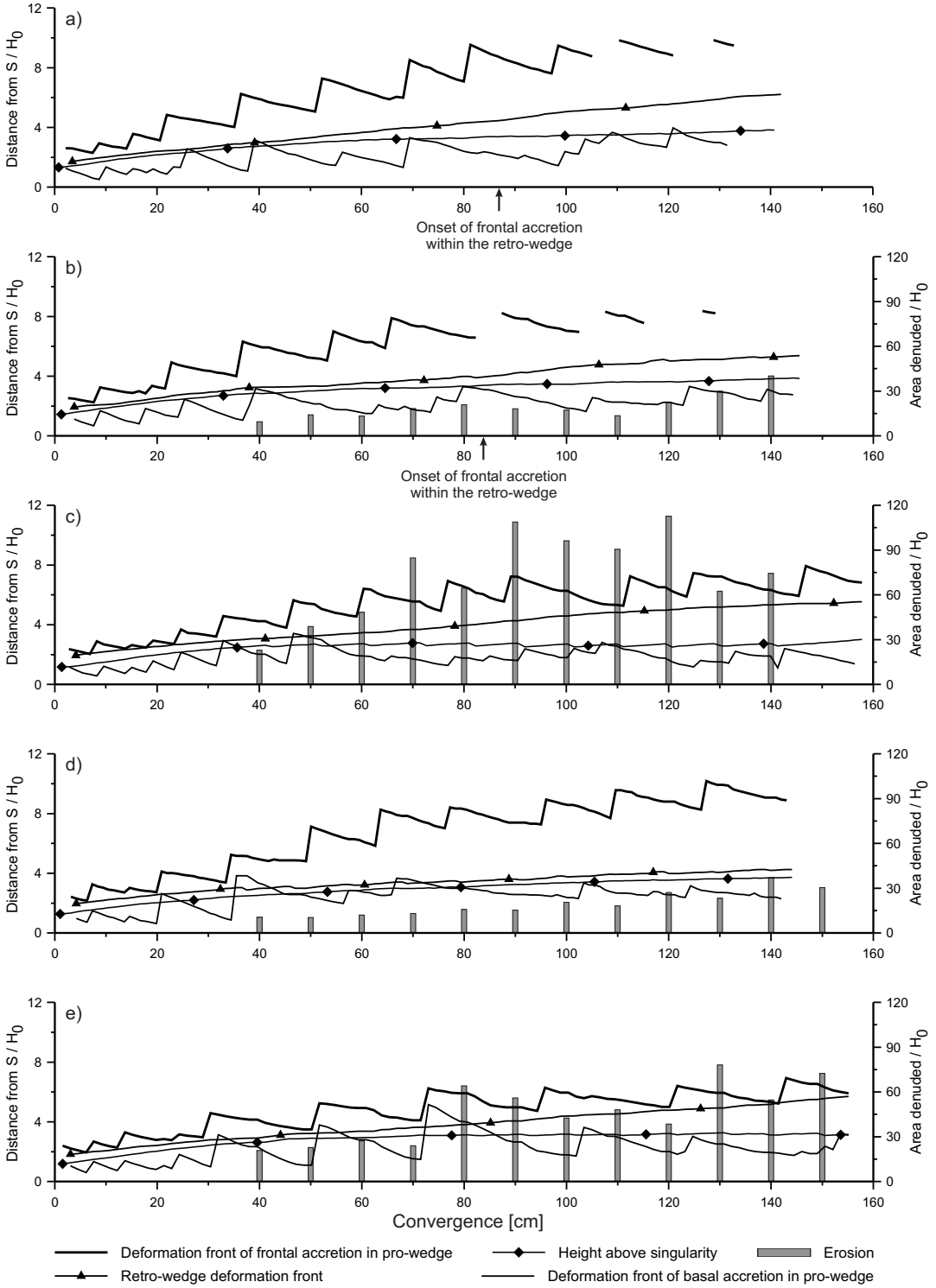

Figure 6.6: Evolution of geometric parameters derived from the PIV images at every 1.5 *cm* of convergence. The amount of eroded material at every 10 *cm* of convergence is given as well. (a) Reference experiment; Distributed erosion of: (b) Retro-wedge, (c) Pro-wedge; Focused erosion of: (d) Retro-wedge, (e) Pro-wedge.

any of the other experiments. Distributed pro-wedge erosion however removed nearly the entire upper sand-unit and thus lead to a dominance of stacked duplexes within the pro-wedge. Only four out of eight thrusts are completely preserved at the final stage of this experiment (Fig. 5.11a, e). This agrees well with the observation that distributed pro-wedge erosion leads to the maximum amount of mass denuded in any of the four erosion experiments (Fig. 6.6, Table 6.1). Also, a mass flux steady state (tectonic advection equals erosion) is reached at two convergence intervals only during this experiment (Fig. 6.6). This is consistent with the observation that the experiment with distributed pro-wedge erosion shows the least flexural deflection (Fig. 6.4). The more general observation derived from figure (6.6), is that the amount of incrementally denuded material increases through time as a consequence of the increase in length of either the pro- or the retro-wedge. It has to be emphasised that the simulated erosion modes assume an ideal-shaped bivergent wedge with a smooth topographic gradient. This however is perturbed by frontal and basal accretion. Thus, the amount of material taken away at any increment of convergence depends on the state within the accretion cycle, i. e., during thrust initiation phases, topography is build up far away from the pro-wedge toe, which results in an overestimation of the material to be denuded. In contrast, during underthrusting phases the envelope of the pro-wedge is much smoother and adjustment of the simulated erosion law to this envelope is more accurate.

Frontal and basal accretion. Similar to the reference experiment time series show that the propagation of frontal accretion is composed of individual accretion cycles (Fig. 6.6). The lateral growth of the pro-wedge as well as the height above the singularity is again best described by power laws. However, the respective power law coefficients are significantly lower than the theoretically predicated value (Table 6.1). Whereas the spacing of frontal accretion, sensu Marshak and Wilkerson (1992), remains fairly constant, the wavelength varies within and between experiments and is thus more sensitive to the parameters tested. The sample standard deviation (s_{fw}) is highest for the experiment with distributed and lowest for the experiment with focused pro-wedge erosion (Table 6.1).

Basal accretion is, in contrast to the very regular propagation of frontal accretion, more irregular in terms of its wavelength and its spacing (Fig. 6.6). The variability expressed in the sample standard deviation of the wavelength (s_{bw}) was calculated for all experiments. It emerges that s_{bw} always exceeds s_{fw}. Also, the range of the latter (0.3) is nearly half the value of the former (0.72) and suggests that basal accretion is more sensitive to the parameters tested (Table 6.1). Convergence intervals, during which both accretion modes are either in or out of phase, are always too short to be correlated over longer distances. There is however, a prominent exception. In the experiment with focused pro-wedge erosion both accretion modes are in phase throughout the entire experiment, which suggests that basal and frontal accretion are not decoupled in time (Fig. 6.6). The respective wavelength of basal accretion remains fairly constant, which is evidenced by the lowest s_{bw}-value among all experiments.

After the first erosion increment, basal accretion propagated towards the foreland in pro-wedge erosion experiments, whereas it stepped back in retro-wedge erosion experiments (Fig. 6.6). The further evolution of basal accretion shows that retro-wedge erosion tends to reduce shorter wavelength activity as compared to the reference or the distributed pro-wedge erosion experiment. During the latter experiment, basal accretion remained nearly stationary with respect to the singularity. It is further pointed out that the height above the singularity can be considered as an envelope for basal accretion (Fig. 6.6). In addition, figure (6.6) reveals that the rate of lateral growth of the pro-wedge during stage III and stage IV is higher for the ref-

Experiment	9.05	9.09	9.10	9.06	9.11
Location of erosion		Pro-wedge		Retro-wedge	
Mode of erosion		Distributed	Focused	Distributed	Focused
Observations					
Flexure	✓	✓	✓	✓	✓
Number of weak layers	1	1	1	1	1
Frontal accretion in retro-wedge	✓	∅	∅	✓	∅
Number of thrusts in pro-wedge after 140 cm of convergence	8	8	6	8	8
Cumulative amount of erosion/H_0	0	804	549	217	233
Sample standard deviation of wavelength of frontal accretion s_{fw}	0.15	0.45	0.18	0.29	0.24
Sample standard deviation of wavelength of basal accretion s_{bw}	0.47	0.48	0.39	0.78	1.11
Power law equation of lateral growth of pro-wedge $y_L =$	$1.06t^{0.44}$	$1.08t^{0.37}$	$1.34t^{0.30}$	$1.17t^{0.40}$	$0.90t^{0.47}$
Coefficient of determination $R^2_L =$	0.89	0.87	0.83	0.89	0.90
Power law equation of height above singularity $y_H =$	$1.03t^{0.26}$	$1.10t^{0.19}$	$1.00t^{0.24}$	$1.12t^{0.24}$	$0.92t^{0.27}$
Coefficient of determination $R^2_H =$	0.97	0.83	0.93	0.98	0.98
Out-of-sequence displacement (OOSD) index	3.73	4.16	0.97	3.42	3.16
Propagation of frontal accretion	0*	—	–	-	-
Propagation of basal accretion		–	0	-	-
Height above singularity		-	-	+	+
Exhumation of frontally accreted material		+	+	0	0
Exhumation of basally accreted material		0	0	+	+
Finite e_{xy} at retro-shear zone		-	0	0	+
Finite e_{xy} at mid-level detachment		–	–	-	+

* Reference level derived from experiment without denudation. - less, + more than reference level.

Table 6.1: Summary of experimentally derived results - 2^{nd} experimental series.

erence and both retro-wedge erosion experiments when compared to both pro-wedge erosion experiments. Lateral pro-wedge growth within the latter is nearly stationary. A summary of the relative magnitudes of the propagation of frontal and basal accretion is given in table (6.1).

Topographic evolution. Similar to the reference experiment, the topography of all erosion experiments consists of two domains, one that comprises the pro-wedge and grows by discrete steps and one that encompasses the axial-zone and the retro-wedge which grow more concentrically (Fig. 6.7). In both retro-wedge erosion experiments this equidistant concentric growth pattern as observed in the reference experiment is perturbed. Lines representing incremental stages of wedge evolution merge at an earlier stage, i. e., after the first erosion increment at 40 cm of convergence, than it is the case for the reference experiment, i. e., after 120 cm of convergence. Parts of the axial-zone and the retro-wedge, which were not subject to the backstepping pro-wedge erosion, tend to retain their equidistant concentric growth in both pro-wedge erosion experiments. The respective pro-wedge slopes are stationary after $\sim 60\,cm$ of convergence (Fig. 6.7).

Both topographic domains are mirrored, similar to the reference experiment, in the corresponding distribution of ISU (Fig. 6.8). The overall evolution of ISU in the retro-wedge erosion experiments and the reference experiment is similar. Thereby, maximum ISU is confined to either initiated or re-activated ramp segments and to the retro-wedge. A change of ISU by one order of magnitude due to thrust re-activation, as shown in section (5.1), can be recognised in both retro-wedge erosion experiments (Fig. 6.8). The experiment with distributed retro-wedge erosion shows a peak in incremental surface uplift at $\sim 90\,cm$ of convergence (Fig. 6.8), which is higher than in the reference experiment. After frontal accretion within the retro-wedge has set in, a significant decrease of ISU within the pro-wedge is observed.

This has been as well observed in the reference experiment. A similar feature, with a lower magnitude and without frontal accretion within the retro-wedge is recognised in the focused retro-wedge erosion experiment. Finally, the surface uplift waves, associated with each accretion cycle were found in both retro-wedge erosion experiments.

Both pro-wedge erosion experiments differ significantly with respect to the spatio-temporal distribution of ISU, from the reference and both retro-wedge erosion experiments. In the distributed erosion scenario nearly the entire pro-wedge is heavily denuded, which corresponds to an equally sized area of low magnitude incremental surface uplift within the pro-wedge. Only minor magnitudinal variations are observed. This general pattern is also found in the focused pro-wedge erosion experiment. However, maximum incremental erosion and surface uplift is highest at the toe of the pro-wedge and decrease towards the axial-zone (Fig. 6.8).

Out-of-sequence displacement. Frontal accretion in all experiments shows a pure forward-breaking or piggy-back thrust sequence although the corresponding displacement along each individual thrust is accumulated at several stages during wedge evolution (Fig. 6.9). The resulting out-of-sequence displacement index (section 5.2) is highest for the distributed pro-wedge erosion experiment and lowest for the focused pro-wedge erosion experiment (Table 6.1). In addition, the cumulative thrust length curves are made up of three segments, which can be linked with the three phases of the accretion cycle (section 5.2).

Strain accumulation. Based on the displacement fields derived from PIV analysis, finite strain after 140 *cm* of convergence was calculated for each experiment (Fig. 6.10). The main structural elements such as the basal and the internal detachment, the retro shear-zone and each thrust imbri-

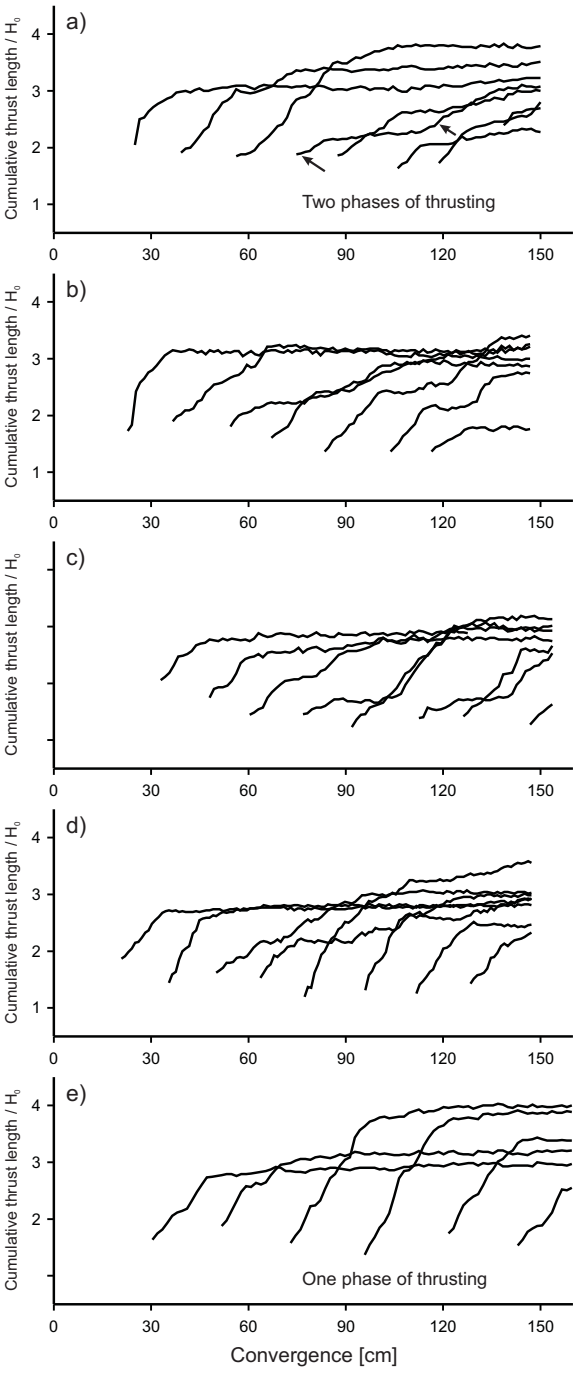

Figure 6.9: Cumulative thrust lengths of each thrust within the pro-wedge, taken at every 1.5 *cm* of convergence. (a) Reference experiment, arrows indicate first and second phase of thrusting; Distributed erosion of: (b) Retro-wedge, (c) Pro-wedge; Focused erosion of: (d) Retro-wedge, (e) Pro-wedge. Experiments (d) and (e) have the least OOSD index.

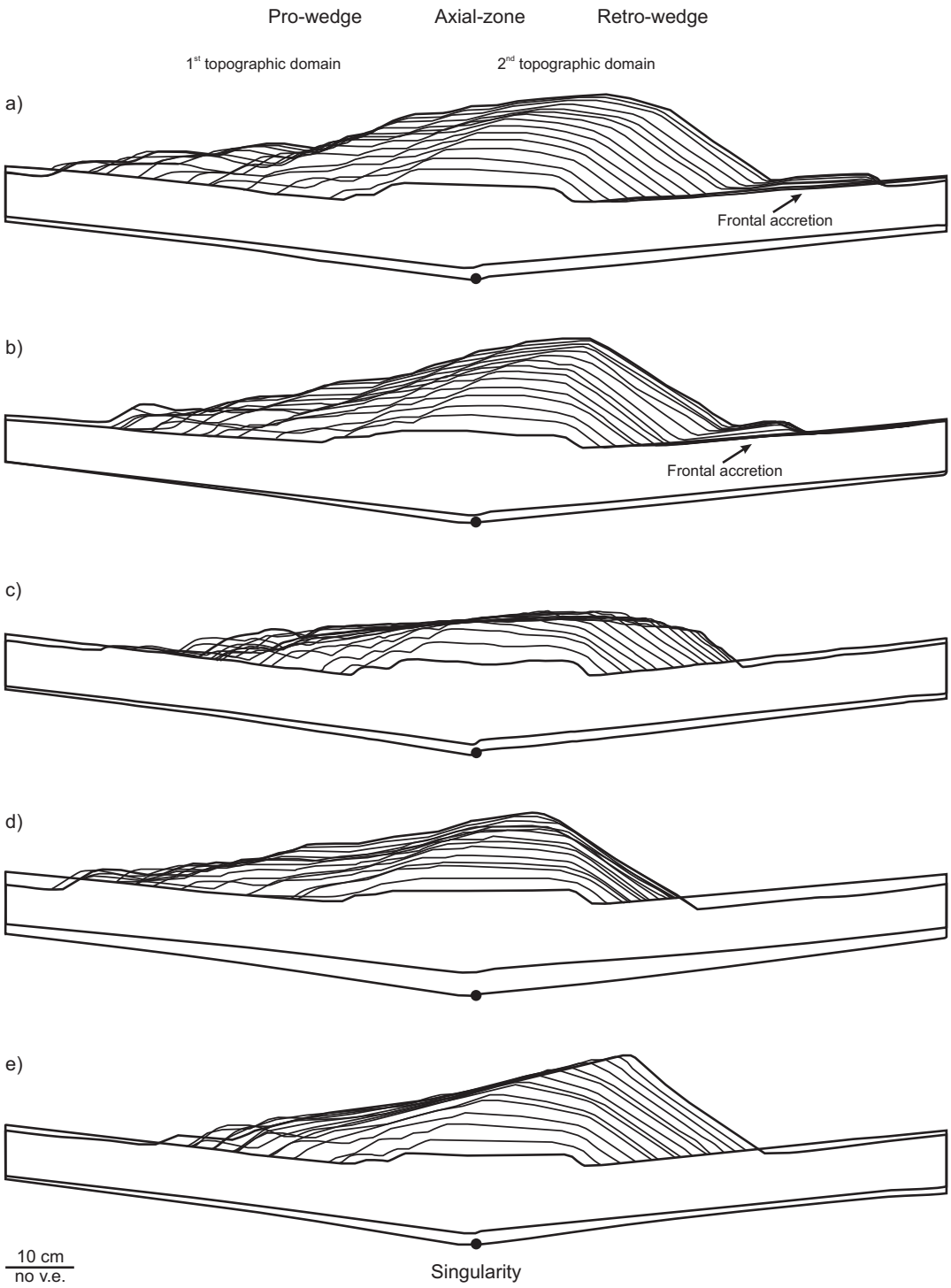

Figure 6.7: Topographic evolution of all experiments of the 2^{nd} series. Outlines were taken at every $10\,cm$ of convergence. The first, i. e., after $10\,cm$ and the last, i. e., after $150\,cm$ of convergence outline are given in complete form, to indicate the magnitude of flexure. (a) Reference experiment; Distributed erosion of: (b) Retro-wedge, (c) Pro-wedge; Focused erosion of: (d) Retro-wedge, (e) Pro-wedge. Pro-wedge slopes in both pro-wedge erosion experiments (c and e) are nearly stationary.

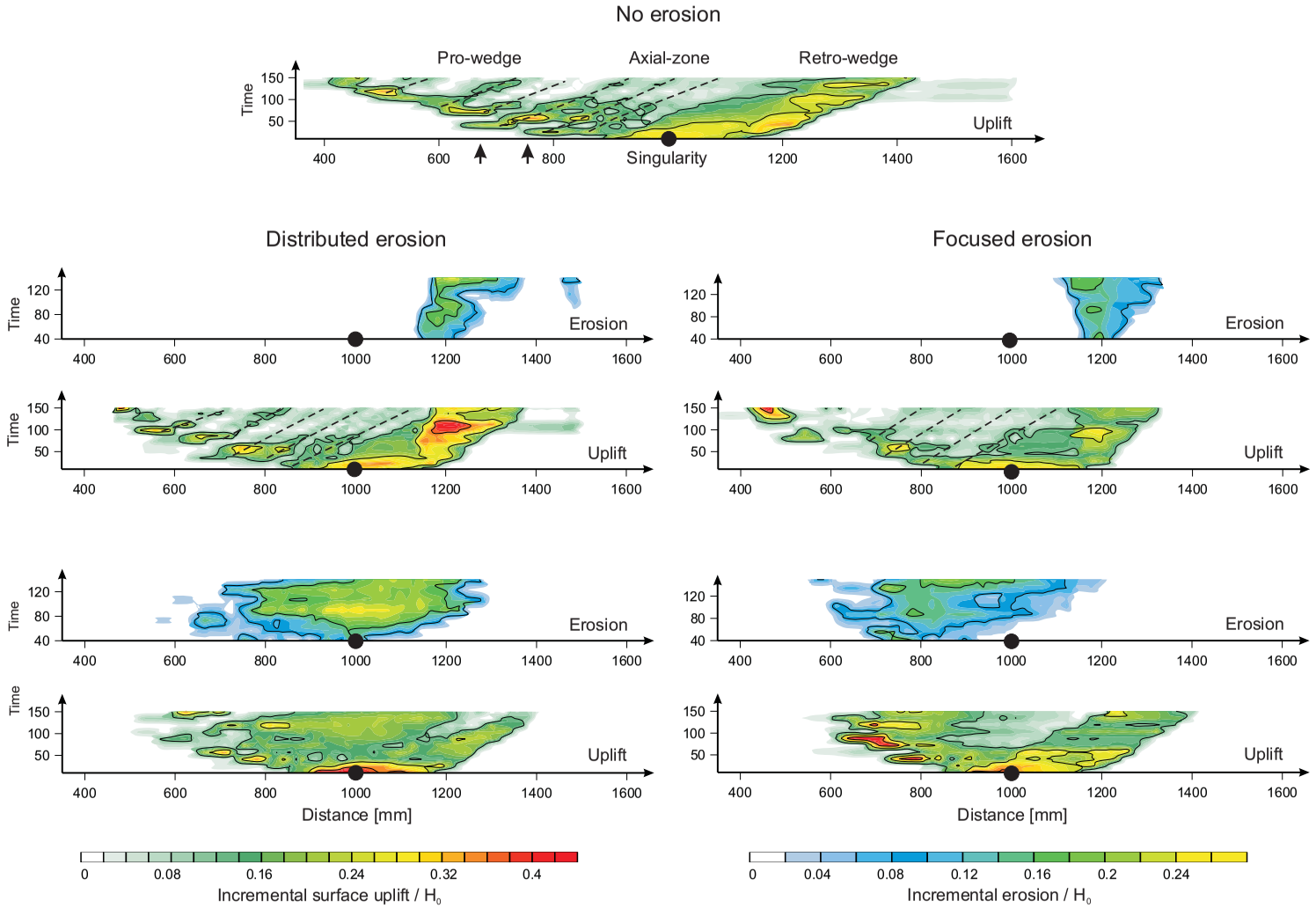

Figure 6.8: ISU and incremental erosion are mapped at every 0.5 *mm* along the experiment (abscissa) and are displayed as a function of time (ordinate). Time is expressed in *cm* of convergence. Data were taken at every 10 *cm* of convergence. Dashed lines trace the initiation and re-activation positions of thrust ramps. Re-activation can lead to a temporary increase of incremental surface ISU by one order of magnitude for a given position. Two examples are highlighted by arrows.

cate as well as the duplexes can be clearly identified for each experiment. A systematic distribution of finite strain accumulated by each individual thrust imbricate can be observed as well. Finite strain is lowest within imbricates closest to the toe of the pro-wedge, and highest in the central part and decreases towards the top. Finally, it is pointed out that the magnitude of retro-shear is highest at the retro shear-zone which separates lower-plate from upper-plate material and is thus interpreted as long-lived.

However, if similar structures are compared between experiments, it can be shown that different magnitudes of finite strain were accommodated in dependence on the location and the mode of erosion. In the experiment with focused retro-wedge erosion the long-lived retro shear-zone accommodated most finite strain relative to all other experiments. This structure accommodated the least magnitude of finite strain in the experiment with distributed pro-wedge erosion. The long-lived retro shear-zones within the remaining three experiments accumulated similar magnitudes of finite strain (Table 6.1). A likewise pattern is found with respect to the magnitude of finite strain accumulated by the internal glass-bead layer. There, finite strain is highest in the experiment with focused retro-wedge erosion and lowest in both pro-wedge erosion experiments (Table 6.1). The accretion cycle with its three phases was observed in all experiments and is thus concordant with the documented surface uplift waves and the cumulative evolution of thrust lengths (Fig. 6.11).

6.3 Discussion

The purpose of this study has been to demonstrate the influence of the location of erosion with respect to the convergence geometry and the mode of erosion, i. e., distributed or focused, on the upper crustal kinematics of bivergent orogenic wedges. Scaled sandbox simulations were chosen to address this issue. Again, we intended to reduce the number of kinematic boundary conditions and to study the most general case, in order to allow a more self-organised growth of the bivergent sand-wedge. It is highlighted here that this study was not aimed at reproducing the geometry of a certain structure or geomorphologic feature. Since the four-staged evolutionary model as well as the accretion cycle have been extensively dealt with in chapter (5), we focus our discussion on the sensitivity of model results with respect to the simulated erosion intervals and on the influence of both tested parameters on bivergent wedge evolution.

6.3.1 Concepts of bivergent wedge evolution and the accretion cycle

The evolution of experiments carried out during the second experimental series supports the postulation of a four-staged evolutionary pathway for bivergent wedges (Fig. 6.6, Fig. 6.4) and the reader is referred back to chapter (5) for further details. In addition, surface uplift waves (Fig. 6.8) in conjunction with the cumulative length evolution of thrusts (Fig. 6.9) and finally the EDM (Fig. 6.11) bear strong evidence that the accretion cycle with its three phases operates in all experiments. This lends additional support to the notion that the first two observations can be used to infer the phase within an accretion cycle, if strain-monitoring techniques such as PIV are not available. As shown in section (5.3.2) this may also hold for “natural” data.

6.3.2 Discrete erosion versus continuous deformation

The simulation of erosion within sandbox experiments remains one of the key challenges to be addressed in the future. At present it is only possible to simulate the effect of erosion, i. e., the distribution of unloading across an orogen and not the process of erosion either by rivers, glaciers or bedrock landslides. Due to practical limitations erosion can only be simulated at discrete time in-

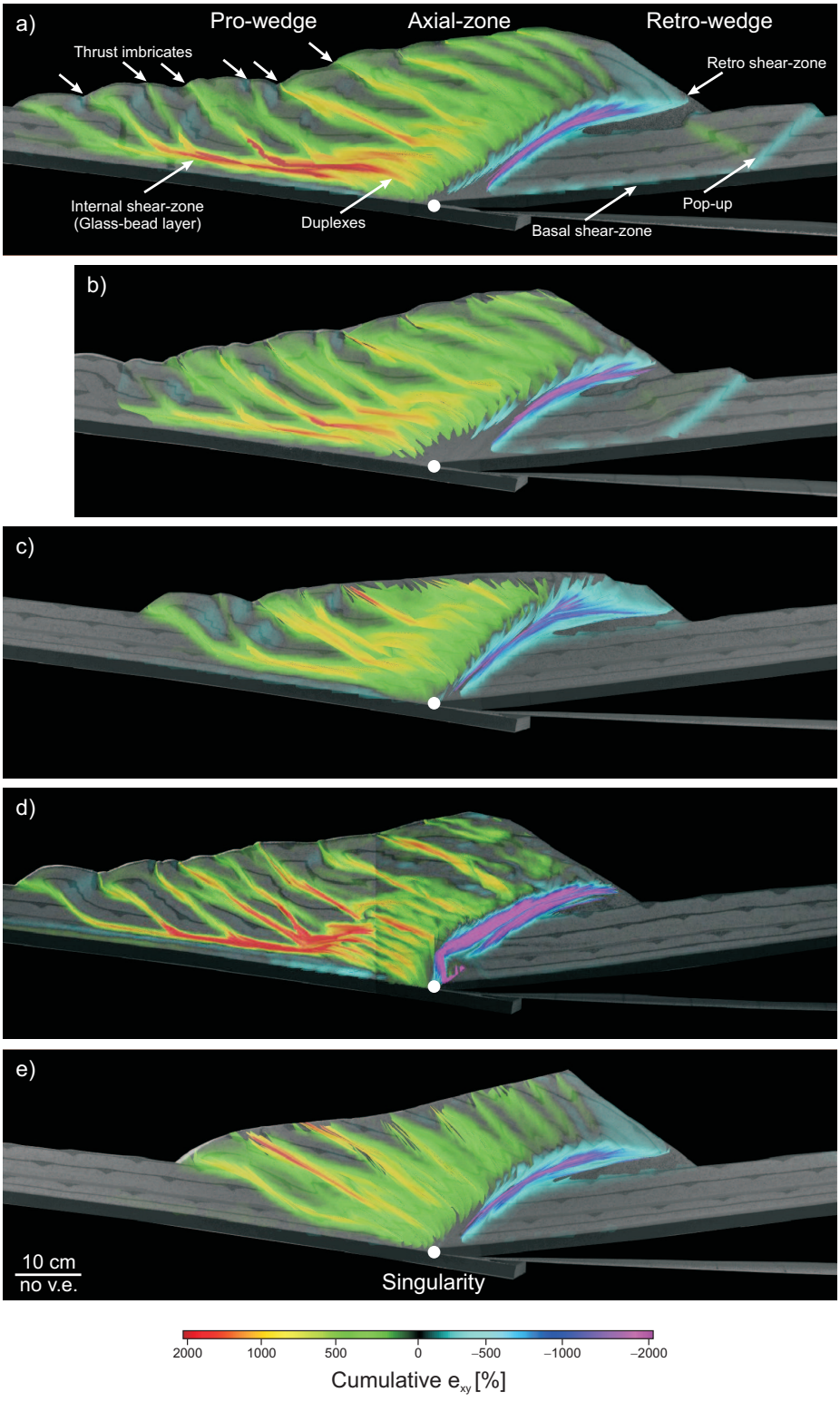

Figure 6.10: Finite e_{xy} after 140 cm of convergence. (a) Reference experiment; Distributed erosion of: (b) Retro-wedge, (c) Pro-wedge; Focused erosion of: (d) Retro-wedge, (e) Pro-wedge. Note the differing magnitudes of finite strain along the retro shear-zone and the glass bead-layer between experiments.

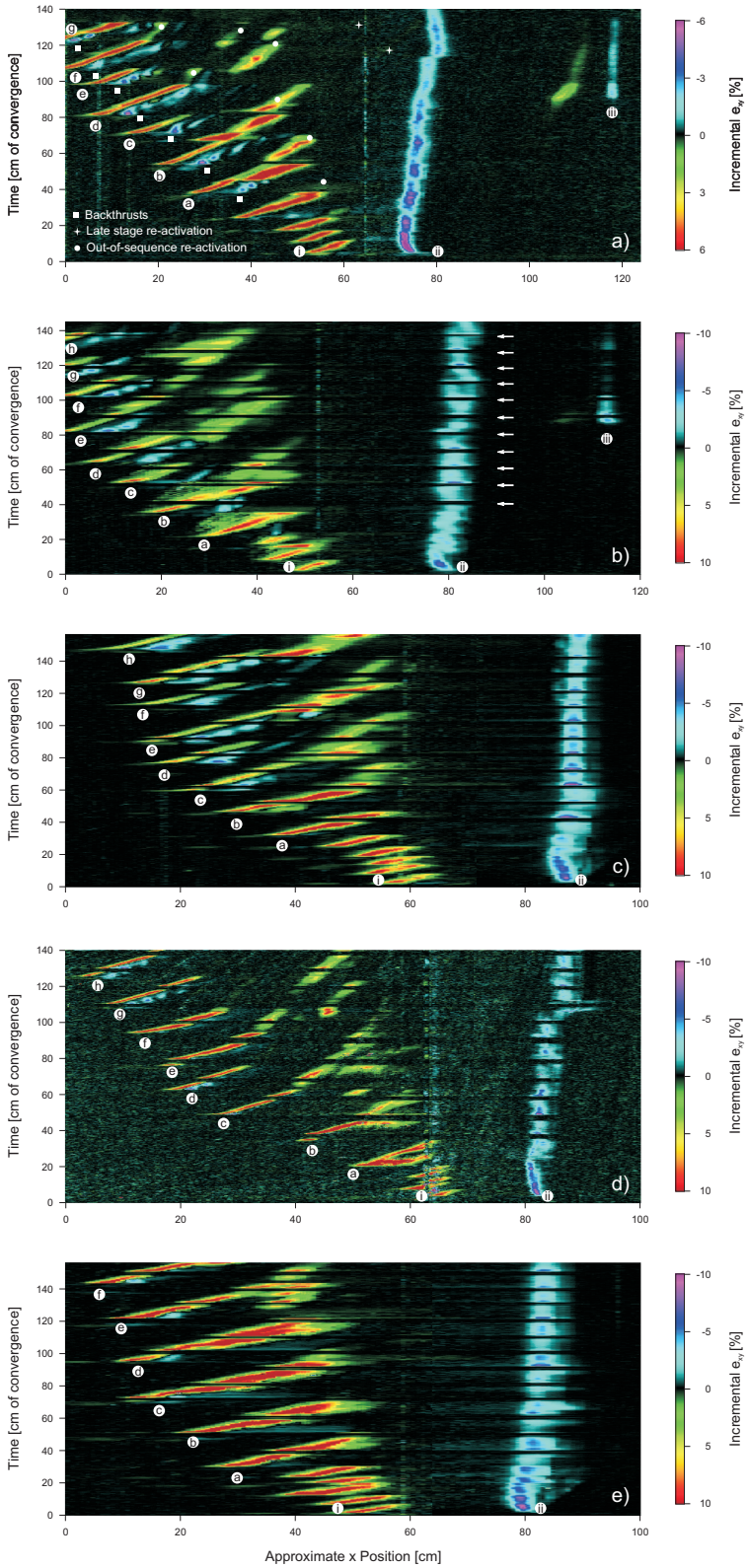

Figure 6.11: Evolution of deformation maps for all experiments of the 2^{nd} experimental series. (a) Reference experiment; Distributed erosion of: (b) Retro-wedge, (c) Pro-wedge; Focused erosion of: (d) Retro-wedge, (e) Prowedge. Labels ⓐ to ⓖ refer to forethrusts within the pro-wedge. ⓘ denotes the pro-shear of the initial pop-up, ⓘⓘ the respective retro-shear and ⓘⓘⓘ denotes the frontal accretion within the retro-wedge. The accretion cycle with its three phases can be recognised in all experiments. Black horizontal lines, pointed to by white arrows in (b) represent times of erosion. For erosion to be simulated, convergence was stopped. Note that no change of incremental e_{xy} accumulation occurs across erosion intervals.

tervals which might be considered artificial with respect to a continuously growing bivergent sand-wedge. If the applied erosion interval controls the evolution of the bivergent sand-wedge, one should expect an immediate response of the wedge with a frequency of the erosion interval. This however, was not recognised in the time series data, excluding the lowering of the height above the singularity. In addition, experiments from Konstantinovskaia and Malavieille (2005), which involve a $1\,cm$ of convergence interval of erosion revealed similar results with respect to the final structural geometries, as presented in this study. We therefore assume that the interval with which the sand-wedge is denuded is of less importance than the mode and location of erosion as shown below.

Furthermore, there is growing evidence that erosion is far more episodic than often implicitly assumed. Storms, floods and landslides show a power-law distribution, which means that the bulk of erosional work is done by high-magnitude, low-frequency events (Fujii, 1969; Noever, 1993; Sugai et al., 1994; Hovius et al., 1997; Stark and Hovius, 2001; Guzzetti et al., 2002). The control of periodic (deglaciation, intense monsoon years, severe El Niños) and episodic (high-intensity rainstorms, earthquakes) processes on erosion has been observed in the Himalayas, in Taiwan, in New Zealand and in Papua New Guinea (Harbor and Warburton, 1993; Densmore and Hovius, 2000; Guzzetti et al., 2002; Dadson et al., 2003; Keefer et al., 2003; Korup et al., 2004; Barnard et al., 2004; Thiede et al., 2004; Ji et al., 2005). Finally, thermochronometric methods can only bracket the time span of an erosion episode. Following this view, Burbank and Beck (1991) speculated that 90 % of erosion may have been accomplished in 10 % of the time. Taken all together we suggest that the erosion approach followed here is justified by the above observations.

6.3.3 Influence of erosion on bivergent wedge kinematics

Crustal-scaled processes of mountain building have been successfully described numerically by minimum work theory (Hardy et al., 1998; Masek and Duncan, 1998; Gutscher et al., 1998; Gerbault and Garcia-Castellanos, 2005) and we therefore propose that the results shown in this study might be explained again in the light of this concept. Following this view, a bivergent sand-wedge subject to erosion has several possibilities to respond to continued convergence by: (i) the initiation of a new thrust either within the upper or the lower plate; (ii) continued slip along the deformation front; (iii) reactivation of one or more internal thrusts; (iv) slip along the retro-shear zone; (v) footwall or hangingwall shortcuts and (vi) internal deformation. Which of these possibilities is "chosen" by the sand-wedge depends on the respective gravitational and frictional work. Whereas the former is controlled by the lateral distribution of erosion, the latter is determined by the strength of the undeformed material, which in turn depends on its thickness, as well as the degree of both strain softening and strain hardening.

This interpretation is exemplified with the propagation of frontal accretion within the pro-wedge. It is evident from figure (6.6) that the spacing of thrusts is fairly constant throughout all experiments, which agrees well with theoretical considerations and results from sandbox simulations (e. g., Bombolakis (1986); Boyer (1995) and section (5.2)). In contrast, the wavelength of frontal accretion, which is defined as the time expressed in convergence between two consecutive thrust initiation events, depends on the mode and location of erosion (Fig. 6.6, Table 6.1). A permanent unloading of the deformation front, as observed in the focused pro-wedge erosion experiment, leads to an increase of slip along successive thrust imbricates, which in turn retards the propagation of deformation into the foreland (Fig. 6.6, Fig. 6.7). Evidence for increased slip during the

focused pro-wedge erosion experiment is derived from the cumulative thrust lengths (Fig. 6.9) and the resulting out-of sequence displacement index, which is the lowest among all experiments. This observation does not contradict predictions either derived from the CCW concept (e. g., Davis et al., 1983) or from sandbox simulations (e. g., Storti et al., 2000), which state that erosion promotes internal deformation. Instead, focused erosion of the very frontal part of the pro-wedge is considered to represent a special case, which has been previously overlooked or not explicitly dealt with. Also, only the experiment with focused pro-wedge erosion exposes the glass-bead layer at the toe of the pro-wedge (Fig. 6.4). Further support for increased slip is derived from the fact that only six imbricate thrusts are needed to accommodate $140\,cm$ of convergence, whereas all other experiments show eight imbricates. This agrees well with observations from other sandbox simulations (Persson et al., 2004), who showed that erosion tends to lengthen the lifetime of individual thrusts.

Focused erosion of the deformation front leads also to a lack of sufficient overthrust length needed to activate the internal glass-bead layer (Kukowski et al., 2002). Thus, frontal accretion by thrust imbrication and basal accretion by duplex formation are in phase throughout the experiment and form one dynamical system. This might explain the observed lowest variability with respect to the wavelength of both accretion modes.

On the contrary, the wavelength of frontal accretion during distributed pro-wedge erosion shows the highest variability (Table 6.1). During this experiment, the highest erosion rates occur at the central and at the rearward part of the pro-wedge. Also, erosion rates at the respective toeward part show a higher degree of variability through time as the corresponding part in the focused pro-wedge erosion experiment (Fig. 6.8). It follows that unloading of the deformation front is more variable through time as well, which in turn influences the wavelength of frontal accretion. Furthermore, in order to restore its critical taper, the pro-wedge deforms internally, i. e., through re-activation of older thrusts. It follows that the propagation of deformation into the foreland is retarded, which agrees with the results from Schlunegger (1999) and Hovius (2000). The preference of internal deformation is mirrored in the diffuse pattern of finite strain and the highest out-of-sequence displacement index among all experiments (Fig. 6.10, Table 6.1) and is thus in accordance with Willett et al. (1993). Depending on the magnitude of internal deformation, propagation of deformation into the foreland is retarded and thus adds to its variability.

Retro-wedge erosion unloads the axial-zone and especially the retro-shear zone, which eases translation of pro-wedge derived material towards the upper plate. It follows that in favour of internal deformation, the propagation of frontal accretion can be retarded. The resultant variability of the respective wavelength is similar for both retro-wedge erosion experiments but higher than the one from the reference experiment (Table 6.1). This highlights the a significant spatial offset between cause (retro-wedge erosion) and response (propagation of deformation within the pro-wedge).

Basal accretion is more sensitive to changes of the load gradient determined by erosion, since the respective thrust spacing and the corresponding wavelengths differ significantly within and between experiments (Fig. 6.6, Table 6.1). The formation of duplexes depends on the load imposed by the frontally accreted material, the rotation of the glass-bead layer resulting from the stacking and backward translation of the duplexes and the load upon the retro-shear zone. As noted above, retro-wedge erosion unloads the axial-zone and especially the retro-shear zone. It follows that duplexes can be more easily stacked and transferred towards the upper plate. Two consequences emerge. At the expense of lateral growth of the pro-wedge, vertical growth of the axial-zone and the retro-wedge is promoted. Despite the fact that

material is removed, both experiments with retro-wedge erosion have a higher elevation above the singularity than the reference or the pro-wedge erosion experiments. This is consistent with the observed acceleration of basally accreted particles (Fig. 6.4) and the prominent maximum in ISU within the retro-wedge (Fig. 6.8). We therefore suggest that retro-wedge erosion enhances particle flow of basal accretion. Note that during pro-wedge erosion frontal accretion is accelerated (Fig. 6.4). A further consequence of the unloading of the axial-zone and the retro-wedge is that longer undeformed sand-sheets can be drawn beneath the internal glass-bead layer towards the singularity until failure occurs and thus reduces shorter wavelength activity. This is consistent with the predictions from minimum work calculations by Gutscher et al. (1998).

Taken all together, our results suggest that the location of erosion with respect to the convergence geometry as well as the erosion mode have a profound effect on the ratio between piggy-back thrusting versus internal deformation. This is supported by a recent study in the Himalayas. Based on $^{40}Ar/^{39}Ar$ and AFT dating, Thiede et al. (2005) showed that pronounced erosion during the last $10\,Ma$ lead to increased rock uplift and exhumation within the central part of the Himalayan pro-wedge in favour of the propagation of deformation towards the southern foreland. Although, the rate of Eurasia-India convergence is thought to have remained constant since that time, the Himalayan deformation front has only migrated 20 to $50\,km$ southward (Thiede et al., 2005).

6.4 Implications and predictions for natural orogens

In this study we have investigated the influence of the location of erosion with respect to the convergence geometry and the mode of erosion, i. e., distributed or focused, which are thought to represent end-members, on the kinematics of bivergent sand-wedges (Fig. 6.12). We re-emphasise the scale-invariance of brittle behaviour and point out that the implications and predictions derived from the second experimental series are not limited to bivergent orogens and may have some bearing for fold and thrust belts as well. Note however, that this study is focused on lower temperature orogens were brittle behaviour prevails. Therefore, some caution must be taken while transferring and applying our results to natural examples. High exhumation rates may finally lead to the removal of the highest strength part of the continental crust, which significantly reduces its integrated strength. At this stage ductile processes might start to dominate (Beaumont et al., 2001; Zeitler et al., 2001; Koons et al., 2002).

Similar to Willett (1999) we predict that the location of erosion with respect to the convergence geometry determines the outcrop pattern of metamorphic facies. We further propose that deformation responds immediately to erosion. Retro-wedge erosion amplifies the displacement of the basally accreted material, whereas pro-wedge erosion accelerates and additionally redirects the particle flow of the frontally accreted material. Pro- and retro-wedge erosion retard the propagation of deformation within the pro-wedge. This effect is stronger for pro-wedge erosion.

The evolution of Borneo is consistent with the last prediction. Strong synkinematic erosion under tropical conditions prohibited the growth of a wide thin-skinned fold-and-thrust belt. The resulting crustal load was not sufficient to generate a foreland basin (Hall and Nichols, 2002). Similarly, Schlunegger and Simpson (2002) demonstrated for the European Alps that a significant decrease in the erosional efficiency during the Early Miocene led to a change from vertical extrusion associated with rapid exhumation during the Late Oligocene to a mainly horizontally directed extrusion, i. e., the formation of the Jura fold and thrust belt and the southern Alps during Middle to Late Miocene times.

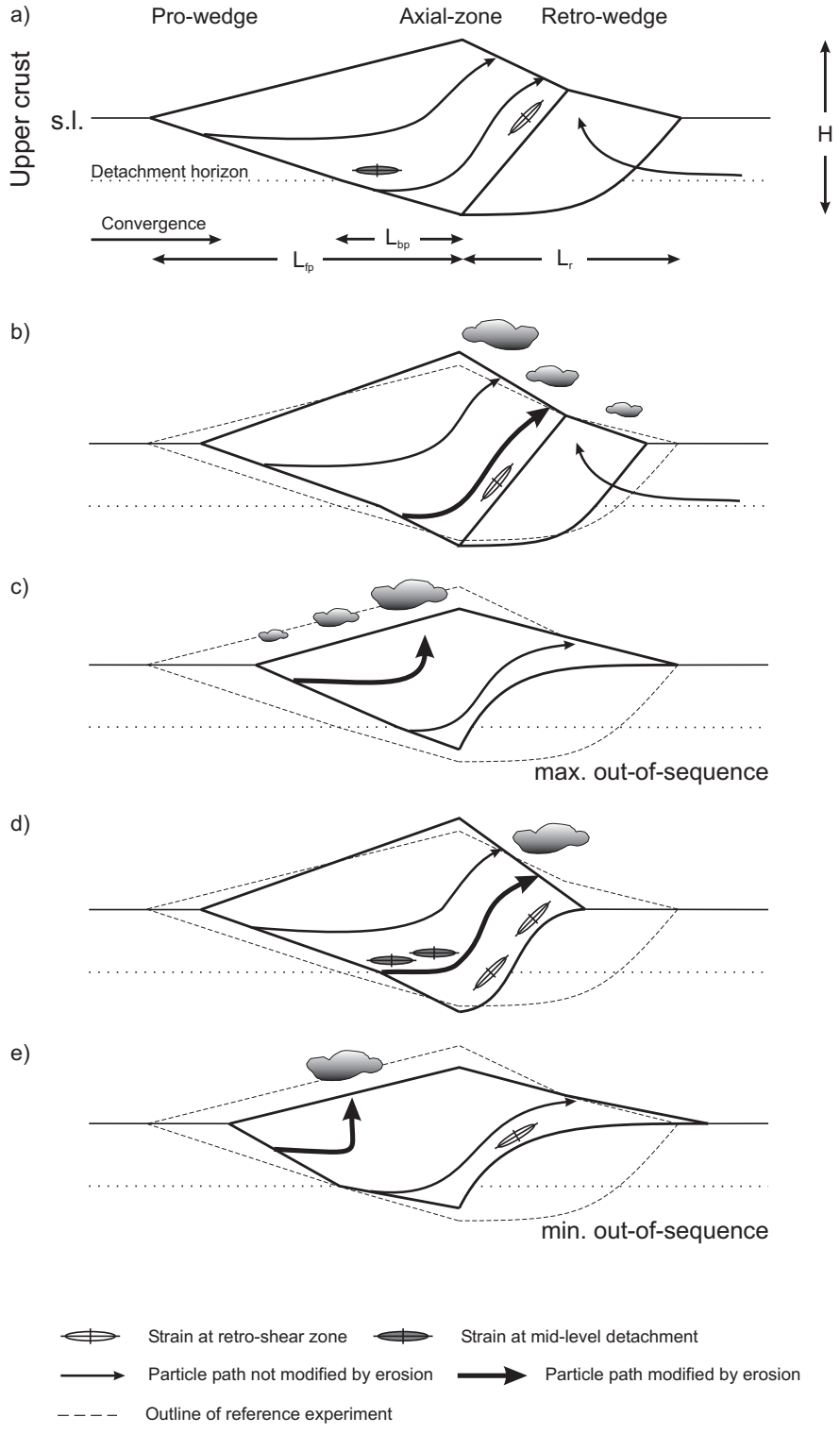

Figure 6.12: Synopsis of results. Outlines indicate trends of bivergent wedge growth in dependence of the location and the mode of erosion. Magnitude and direction of schematic particle paths, as well as locations of high finite strain are given. Schematic particle are derived from ~ 120 calculated particle paths as given in Fig. 6.5d. (a) Reference experiment; Distributed erosion of: (b) Retro-wedge, (c) Pro-wedge; Focused erosion of: (d) Retro-wedge, (e) Pro-wedge.

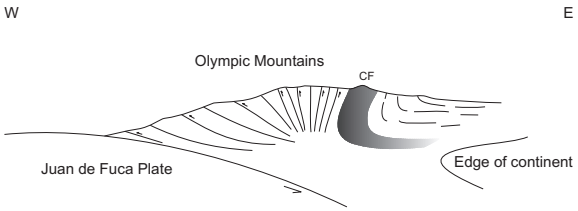

Figure 6.13: Generalised section through the Olympic Mountains as postulated from field work. Subduction of the Juan de Fuca plate beneath North America results in the formation of an accretionary complex - Olympic Mountains. Note rotation of forethrusts and the absence of a prominent backthrust, which has also not been imaged on seismic profiles (Brandon and Calderwood, 1990). CF, Crescent Formation, which may have acted as a backstop. The Olympic Mountains are assumed to be in a mass steady-state since $\sim 14\,Ma$ (Pazzaglia and Brandon, 2001). Modified after Tabor and Cady (1978).

Also, we suggest that retro-wedge erosion amplifies vertical growth and leads to strain accumulation along the retro shear-zone and the mid-level-detachment. This indicates that for retro-wedge erosion cause (erosion) and response (deformation) are significantly offset in space. Thus, the cause for a certain seismicity pattern observed in the pro-wedge might be the eroding retro-wedge, hundreds of kilometers away. In contrast, pro-wedge erosion evokes a complete decoupling of the retro-wedge from the pro-wedge. Here cause and response are spatially more closely related. Both results highlight the need for orogen-wide climate-tectonics studies.

Intense erosion of the rearward part of the pro-wedge and the adjacent axial-zone may result in a faning of the retro-shear zone, i. e., slip is taken up by an array of retro-shear zones rather than one single, long-lived structure. This might explain why no prominent backthrust has been documented from the Olympic Mountains, which are assumed to be in a mass steady-state for the last $\sim 14\,Ma$ (Brandon and Calderwood, 1990; Pazzaglia and Brandon, 2001). Instead, Tabor and Cady (1978) point out that several vertical thrusts take up slip (Fig. 6.13). We found that more focused erosion is associated with a more focused tectonic response. This interpretation is supported by observations from the Chugach/St. Elias Range in Southern Alaska. There, the windward position of the ELA coincides with a narrow zone of active upper plate deformation associated with high rates of rock uplift (Meigs and Sauber, 2000; Sheaf et al., 2003). Also, strong fluvial erosion in both Himalayan syntaxes has lead to high exhumation and deformation rates (Zeitler et al., 2001).

A change from distributed to focused erosion may lead to a continued activation of a certain structure, e. g., deformation front and may thus retard the propagation of deformation into the foreland and may also determine which detachment layer is favoured.

Although all of our sandbox simulations exhibit a clear forward breaking or piggy-back sequence of thrusting, considerable displacement is accumulated out-of-sequence by re-activation of older thrusts. The magnitude of the latter is strongly controlled by the location and mode of erosion. Within this respect it is interesting to note, that Mouthereau et al. (2001) showed that the increase of erosion rates was associated with an increase of the number of re-activated or out-of-sequence thrusts in the Taiwan fold and thrust belt. Similarly, Hodges et al. (2004) demonstrated that strong orographic forcing of precipitation lead to concentrated erosion and out-of-sequence thrusting in the Higher Himalayan Ranges.

Finally, we speculate that a bivergent wedge is very robust with respect to its boundary conditions, e. g., mechanic stratigraphy and erosion. Erosion modifies but does not inhibit the segmentation of a bivergent wedge or the simultaneous propagation of frontal and basal accretion. This gains support from a recent study in the Himalayas where the tectonic displacement field is focused by erosion but does not mimic its asymmetric distribution (Burbank et al., 2003). If however, a certain threshold is either exceeded or reached, the kinematics might change their mode.